

Poles Isolation via ESPRIT for Ultra-Wide Band Breast Cancer Imaging

Ahmed M. Abed^{1, 2, *}, Dheyaa T. Al-Zuhairi³, Kaydar Quboa²,
John M. Gahl¹, and Naz E. Islam¹

Abstract—In this paper, microwave breast cancer detection is investigated using the Ultra-Wide Band (UWB) radar imaging technique. A novel calibration approach based on the Estimation of Signal Parameters via Rotational Invariance Technique (ESPRIT) is used and adapted to work in this field. Using this method, many high amplitude undesired responses can be removed like early time clutter, late time clutter, and the mutual coupling between antennas. Using an electromagnetic simulation tool, a numerical phantom with a heterogeneous structure and dispersive dielectric properties is made for simulating the interactions of the electromagnetic fields with various breast tissues and investigating the proposed approach. The calibrated signals show the capability of the proposed algorithm in separating the tumor/glandular responses from the clutter. Also, the results of the proposed algorithm are compared with the Wiener algorithm results which are considered one of the best techniques to remove clutter, reduce late time clutters in the multistatic, and enhance the beamformer algorithm performance. Moreover, we propose the use of Transmitting-Receiving Antenna Separation Distance (TRASD) to limit the reflection angles from the voxel under the calculations of DAS and IDAS beamforming algorithms.

1. INTRODUCTION

Many research groups have investigated Ultra-Wide Band (UWB) imaging techniques through the two previous decades. These approaches typically involved illuminating the breast with a UWB pulse, and then measuring the backscattered signals and processing them. Many approaches were proposed for breast cancer detection that rely on UWB microwave imaging based radar approaches, such as Microwave Tomography (MWT) techniques [1–4], Confocal Microwave Imaging (CMI) [5, 6], microwave imaging via space-time beamforming [7], tissue sensing adaptive radar [8], and channel-ranked beamformer [9]. All these approaches are based on the signal processing approach of the Delay And Sum (DAS) beamforming algorithm [5, 10]. A common approach for confocal microwave imaging is based on the signal processing approach of the Delay-Multiply And Sum (DMAS) beamforming algorithm [11]. Yin et al. [12] introduced a novel Robust and Artifact Resistant (RAR) algorithm, used for monostatic manner. RAR algorithm uses a neighborhood pairwise correlation-based weighting to overcome the adverse effects from both artifact and glandular tissues.

The performance of the microwave approach depends largely on the dielectric contrast between the normal and cancerous tissues at UWB microwave frequencies. In this context, a large scale study done by Lazebnik et al. [13, 14] has shown a high dielectric contrast between the normal adipose and fibroglandular/fibroconnection tissues with a ratio of 10 : 1; however, this study has also shown that the dielectric contrast between the fibroglandular/fibroconnection and malignant tissues is not more than 10% or less. Thus, these studies have indicated a much more difficult imaging scenario since

Received 20 May 2019, Accepted 10 August 2019, Scheduled 26 August 2019

* Corresponding author: Ahmed Maher Abed (amabt7@mail.missouri.edu).

¹ ECE Department, University of Missouri-Columbia, W1024 Lafferre Hall, Columbia, MO 65201, USA. ² Electrical Engineering Department, University of Mosul, Mosul 41002, Iraq. ³ College of Engineering, University of Diyala, Baqubah 32001, Iraq.

the clutter, coming from fibroglandular/fibroconnection tissues, is significantly high. Consequently, the constructive addition of the backscattered signals is potentially much more difficult than previously assumed. However, since the breast is predominantly composed of the adipose tissue, and it is relatively small in size, UWB signals are practically able to penetrate it, but more sophisticated algorithms are needed for image construction and cancer detection.

UWB radar imaging, in the transmitting and receiving method, is typically divided into three types: the monostatic, bistatic, and multistatic methods. The advantage of the monostatic method is the avoidance of mutual coupling among the antennas, which is a significant problem in the cases of bistatic and multistatic methods. Also, the monostatic method has another advantage which is the ease of the early time clutter removal; however, this method has less diversity and smaller channel number than the other two methods. On the other hand, the multistatic method has two main advantages. First, it has more channels which increases the tumor signal power to clutter and noise power ratio at the receiver. Second, more channel diversity is obtained, which gives more information about the tumor since the propagation directions and transmitting/receiving locations will be more diversified. The main disadvantage of this method is the mutual antenna coupling among the antennas and skin reflections that severely degrade signal to clutter ratio. In the same way, the bistatic method contains the disadvantage of the multistatic method, but it has a smaller channel number. Thus, in this paper, we use the multistatic method.

This paper aims to remove clutter forms in the multistatic signals. A frequency domain approach based on the Autoregressive-Moving-Average ARMA signal model was used by Maskooki et al. [15]. They used it for identifying and removing large power signals. However, they preadapted the signals using a typical phantom to identify most early high clutter signals. This assumption will lead to a large effect on the tumor signals. Therefore, we propose the use of another algorithm based on the ESPRIT algorithm, which is well known for its accuracy and calculation efficiency. The adapted ESPRIT algorithm has the power to work on each signal alone for identifying the high amplitude clutters to be removed without any preprocessing.

2. SIGNAL CALIBRATION

A problem in the UWB imaging of breast cancer is the strong backscattering from the breast skin and other reflectors from inside and outside the breast. These backscatters have a negative effect on the reconstructed image since their amplitudes are several orders larger than the backscattered signals from the tumor. This backscatter should be eliminated if possible or minimized before any beamforming process. The backscattering signals must be calibrated to remove/reduce the early and late time clutter. The early time signals in the monostatic system predominantly consist of antenna mismatches reflections, coupling media — skin boundary reflections and the skin — breast tissue boundary reflections, whereas the antennas coupling, as well as the coupling media — skin boundary reflections, and the skin — breast tissue boundary reflections dominate the early time signals in the bistatic or multistatic system.

To remove/reduce these early time clutters, several signal processing algorithms were used such as Averaging [5], Weiner Filter [7], Entropy Filter [16], Hybrid approaches [17], Pole Removal [15], and Independent Component Analysis [18].

In this paper, we propose the use of the Estimation of Signal Parameters via Rotational Invariance Technique (ESPRIT) algorithm to remove strong backscatters. The ESPRIT algorithm is known for its accuracy and computational efficiency.

In addition to the early time signals, there are late time clutters, which are the result of the tissues diversity having different dielectric properties, such as fat-fibroglandular/fibroconnection tissue boundary reflections. The late time clutters cannot be removed since they have low magnitude like the tumor signals, but we can reduce them using Transmitting-Receiving Antennas Separation Distance (TRASD) as will be explained in Section 7.

3. POLES ISOLATION VIA ESPRIT

Poles Isolation via ESPRIT (PI-ESPRIT) algorithm is a frequency domain approach [19]. It is supposed that each scatterer inside or outside the breast will reflect the incident signal with a certain amplitude

and phase; therefore, each scatterer represents a pole in the transfer function, where the backscattering signal is analyzed as an output of a system. The poles that have high magnitude will be canceled (such as the skin reflections and other high amplitude scatters) even if they are received at a late time. This method will improve the detection of the tumor in the sense of the tumor to clutter response ratio.

The algorithm adopted in this paper is based on Magnetic Resonance Spectroscopic Imaging (MRSI), which is also built on the assumption that each scatterer represents a pole. ESPRIT can remove the mutual coupling and other high amplitude signals. The following section begins by deriving a simplified signal model to serve as a background and establish a common expression. This model is established in the context of radar signal processing, and then it will be generalized to the breast cancer detection via a simple substitution of variables.

3.1. Target Impulse Response

Keller's Geometric Theory of Diffraction (GTD) states that the backscattered field from a complex surface tends to be well approximated by a set of discrete scattering centers, and each scatterer center reflects the incident signal with a specific strength b_s and EM propagation delay τ_s that is equal to the time for a round trip of the targets distance r_s at phase velocity of light inside the medium of interest v_{ph} . To describe the scenario analytically, the frequency response could be represented in the following form:

$$G(f) = \sum_s A_s(f) \exp\left(-2\pi j f \frac{2r_s}{v_{ph}}\right) \quad (1)$$

Equation (1) is also known as Fourier Transform of the target's impulse response where $A_s(f)$ is the Fourier Transform of b_s , and $A_s(f)$ is the frequency dependent function corresponding to the s th scattering point. This frequency dependence function is of the form f^α , and the exponent α is known for some common scattering mechanisms. For example, a flat plate has $\alpha = 1$, and a sphere will have $\alpha = 0$. As stated by Cuomo et al. [20], f^α scattering behavior can be accurately estimated by exponential functions over a finite bandwidth interval, so the following Equation (2) can represent the frequency behavior of the reflected signal given in Eq. (1) above.

$$G(f) = \sum_s a_s \exp - \left(\alpha_s + j \frac{4\pi r_s}{v_{ph}} \right) f \quad (2)$$

But these quantities are sampled at identified intervals T in the course of digital signal processing. Therefore, f is replaced with $n\Delta f$ to represent the fact that the system only reflects some discrete frequency set where n represents a particular frequency of the set, and Δf represents the sampling frequency and is equal to $1/T$.

$$G(n) = \sum_s a_s \exp - \left(\alpha_s + j \frac{4\pi r_s}{v_{ph}} \right) n\Delta f \quad (3)$$

3.2. The Exponentially Damped Sinusoidal (EDS) Model

A single-channel with a noiseless time-domain signal having N complex samples x_n , $n = 0, 1, \dots, N - 1$ represents a time series that can be formed as a finite sum of K different exponentially damped complex sinusoids [21]:

$$x_n = \sum_{k=1}^K a_k \exp \{j\varphi_k\} \exp \{(-\alpha_k + j\omega_k) n\Delta t\} \quad (4)$$

where $n\Delta t$ is the time gap between the time origin and sample x_n , whereas Δt is the sampling time interval. a_k represents the amplitudes; φ_k are the phases; α_k are the damping factors; and ω_k are the pulsations. Equations (3) and (4) have a similar mathematical structure. This means that the mathematics of the impulse response of a linear system in Eq. (4) can be used to estimate the parameters of the frequency response of the backscattered signal in Eq. (3).

4. SIGNAL POLES ESTIMATION METHODS

In recent decades, many techniques have been developed to estimate the signal poles z_k using a model function. A well-known subspace-based algorithm ESPRIT-Estimation of Signal Parameters via Rotational Invariance Techniques utilizes the rotational invariance of signal subspaces. ESPRIT uses the Eigen Value Decomposition EVD of the sample covariance matrix, and it is based on the total least squares (TLS) solution. Also, the equivalence between the Singular Value Decomposition (SVD) of the Hankel data matrix and the EVD of the sample covariance matrix is exact. In the Magnetic Resonance Spectroscopic (MRS) literature, the data matrix equivalence of ESPRIT is known as HSVD, and the data matrix equivalent of TLS-ESPRIT is known as HTLS [22]. Although it is suboptimal, according to Papy et al., the HTLS algorithm was proven to be a robust and reliable algorithm as well as easy to implement. Principally, it can be achieved by placing N samples of signal x_n in an $M \times L$ Hankel matrix H and computing the Singular Value Decomposition (SVD) of H . Then K left most singular vectors of the left singular vector matrix are used to retrieve the model parameters. This algorithm is typically applied to the single-channel.

4.1. Hankel Total Least Squares Method HTLS

The process of finding the system poles involves forming a forward prediction or Hankel matrix from the frequency response of the data samples of the backscattered signal, and the frequency response samples are arranged into $M \times L$ Hankel matrix as follows:

$$H = \begin{pmatrix} y(1) & y(2) & y(3) & \cdots & y(L) \\ y(2) & y(3) & \ddots & & y(L-1) \\ y(3) & \ddots & & \cdots & y(L-2) \\ \vdots & & & & \vdots \\ \vdots & & & & \vdots \\ y(N-1+L) & \cdots & \cdots & & y(N) \end{pmatrix} \quad (5)$$

where $y(i)$ are the samples of the frequency domain response of the backscattered data; N is the number of data samples; L is chosen as $N/2$ and $M = N - 1 + L$. This Hankel matrix can be straightforwardly decomposed in a product of three matrices [12]:

$$H = \begin{pmatrix} 1 & \cdots & 1 \\ z_1^1 & \cdots & z_K^1 \\ z_1^2 & \cdots & z_K^2 \\ \vdots & \vdots & \vdots \\ z_1^M & \cdots & z_K^M \end{pmatrix} \begin{pmatrix} c_1 & & 0 \\ & \ddots & \\ 0 & & c_K \end{pmatrix} \begin{pmatrix} 1 & z_1^1 & z_1^2 & \cdots & z_1^L \\ \vdots & \vdots & \vdots & \cdots & \vdots \\ 1 & z_K^1 & z_K^2 & \cdots & z_K^L \end{pmatrix} = SCT^T \quad (6)$$

Equation (6) is called a Vandermonde decomposition (VDMD), and its poles z_K are named generators, whereas Vandermonde vectors are column vectors of S and T . The rank deficiency of H is also computed by the SVD which is defined as follows:

$$H = (U_{sn} \ U_n) \begin{pmatrix} \Sigma_{sn} & 0 \\ 0 & \Sigma_n \end{pmatrix} \begin{pmatrix} V_{sn}^H \\ V_n^H \end{pmatrix} \quad (7)$$

where subscripts 'sn' and 'n' refer to the signal-noise and noise subspaces, respectively; $U_{sn} \in C^{M \times K}$, $U_n \in C^{M \times (M-K)}$, $\Sigma_{sn} \in R^{K \times K}$ contains K non-zero singular values of the signal in a decreasing order of magnitude, where C and R are symbols used in matrix notation to refer to a Complex or Real number matrix, respectively. Also, $\Sigma_n \in R^{(M+1-K) \times (L-K)}$, $V_{sn} \in C^{M \times K}$, $V_n^H \in C^{K \times (M-K)}$, and H denotes the complex conjugate and transpose. In the absence of noise Σ_n is a null matrix, and the SVD of H is reduced to the product $U_{sn} \Sigma_{sn} V_{sn}^H$. The columns of S (respectively T) span the same subspace as the

columns of U_{sn} (respectively V_{sn}). If the signal is corrupted by noise, Σ_n is full rank. Removing the noise part in the presence of a reasonable level of noise, the truncated SVD of H is:

$$H = U_{sn} \Sigma_{sn} V_{sn}^H \quad (8)$$

which is the best rank- K approximation of H and can be considered as a denoised version of H although it is not a Hankel matrix anymore. In this case, the column vectors of U_{sn} yield a good approximation of the subspace spanned by the Vandermonde vectors.

4.2. Shift-Invariance Property and Harmonic Retrieval via Total Least Squares Solution

The matrices S and T possess a shift-invariance property that can be expressed as:

$$S_{\downarrow} Z = S^{\uparrow} \quad (9)$$

and

$$T_{\downarrow} Z = T^{\uparrow} \quad (10)$$

where the up/down arrow placed behind the matrices stands for deleting the top/bottom row of the considered matrix and $Z = \text{diag}(z_1, z_2, \dots, z_K) \in C^{K \times K}$. In the noise-free case, U_{sn} equals S up to a multiplication by a square nonsingular matrix $Q \in C^{K \times K}$:

$$U_{sn} = SQ \quad (11)$$

The matrices U_{sn}^{\uparrow} and U_{sn}^{\downarrow} are related to the Vandermonde matrices S^{\uparrow} and S_{\downarrow} , respectively, in the following way:

$$U_{sn}^{\uparrow} = S^{\uparrow} Q \quad (12)$$

$$U_{sn}^{\downarrow} = S_{\downarrow} Q \quad (13)$$

Combining Equations (9), (10), and (12), Equation (13) results in the shift-invariance property of U_{sn} :

$$U_{sn}^{\uparrow} = U_{sn}^{\downarrow} Q^{-1} Z Q = U_{sn}^{\downarrow} \tilde{Z} \quad (14)$$

where

$$\tilde{Z} = Q^{-1} Z Q$$

The same context applies to the matrix V_{sn}^H . In the case of white noise, the equality does not hold anymore, and there are two sense approaches of the over determined set of linear equations $U_{sn}^{\uparrow} \approx U_{sn}^{\downarrow} \tilde{Z}$:

- The LS solution is given by:

$$\tilde{Z} = \left((U_{sn}^{\uparrow})^T U_{sn}^{\uparrow} \right)^{-1} \left((U_{sn}^{\uparrow})^T U_{sn}^{\downarrow} \right) \quad (15)$$

- Total Least Squares (TLS) that is sensed by:

$$\tilde{Z} = -W_{12} W_{22} \quad (16)$$

where

$$W = \begin{pmatrix} W_{11} & W_{12} \\ W_{21} & W_{22} \end{pmatrix}$$

which is obtained from the SVD of the matrix $(U_{sn}^{\uparrow} U_{sn}^{\downarrow})$:

$$(U_{sn}^{\uparrow} U_{sn}^{\downarrow}) = PLW^H \quad (17)$$

where $P \in C^{M \times 2K}$ is the left singular vector matrix, $W \in C^{2K \times 2K}$ the right singular vector matrix, and $L \in R^{2K \times 2K}$ the (diagonal) singular value matrix.

Once \tilde{Z} is estimated, the complex amplitudes can be estimated by solving the set of equations:

$$\begin{pmatrix} 1 & \cdots & 1 \\ \tilde{z}_1^1 & \cdots & \tilde{z}_K^1 \\ \tilde{z}_1^2 & \cdots & \tilde{z}_K^2 \\ \vdots & \vdots & \vdots \\ \tilde{z}_1^M & \cdots & \tilde{z}_K^M \end{pmatrix} \begin{pmatrix} c_1 \\ c_2 \\ c_3 \\ \vdots \\ c_K \end{pmatrix} = \begin{pmatrix} y(1) \\ y(2) \\ y(3) \\ \vdots \\ y(M) \end{pmatrix} \quad (18)$$

In the Least Squares (LS) sense, Eq. (18) can be solved by:

$$\tilde{C} = \left((\tilde{S})^T \tilde{S} \right)^{-1} \left((\tilde{S})^T Y \right) \quad (19)$$

This summarizes the HTLS algorithm.

After pole definition, R poles will remain; then, for retrieving the frequency response (Y) of the backscattering signal, the following equation will be applied in the ESPRIT approach:

$$\begin{pmatrix} 1 & \cdots & 1 \\ \tilde{z}_1^1 & \cdots & \tilde{z}_R^1 \\ \tilde{z}_1^2 & \cdots & \tilde{z}_R^2 \\ \vdots & \vdots & \vdots \\ \tilde{z}_1^M & \cdots & \tilde{z}_R^M \end{pmatrix} \begin{pmatrix} c_1 \\ c_2 \\ c_3 \\ \vdots \\ c_R \end{pmatrix} = \begin{pmatrix} y(1) \\ y(2) \\ y(3) \\ \vdots \\ y(M) \end{pmatrix} \quad (20)$$

The frequency domain signal is then converted back into the time domain using the inverse-FFT algorithm with the real part only.

In contrast to other algorithms, ESPRIT identifies high amplitude signals to be subtracted from the original signal. This is done by choosing Σ_{sn} in Equation (7) that almost represents these clutters. However, choosing the number of eigenvalue (Σ_{sn} rank) that represents the high amplitude signals is the trickiest problem in this algorithm. Choosing a large rank of Σ_{sn} allows the algorithm to identify the high amplitude signals very accurately, but it may affect the tumour signal. On the other hand, choosing a low rank value leaves some parts of the high amplitude signals undetected which degrade the image quality. Hence, the reconstructed signal will only contain the contributions from the antennas coupling clutter, tumor, and/or Fibroglandular/Fibroconnection signal.

To keep the tumor signal unaffected, we choose a small rank value for Σ_{sn} . This results in some residues generated from the subtraction seen clearly at the early time of the signal. To remove these residues, we apply ESPRIT again but in a reverse manner to the one above when choosing the poles. Here, we choose the lowest values of Σ_n , and this will almost remove the residues generated in the first step. Since our work does not include white noise, we do not worry about the lowest values. By this process, we get the final signal leaving the tumour and glandular signal dominant.

5. WIENER FILTER

To compare our calibration approach with another familiar approach, we use a Wiener filter described in [23] as a calibration approach that has been considered effective by [24, 25] among the other calibration approaches. To apply a Wiener filter in multistatic, we need to find similar channels to allow the Wiener filter to find common information among them. We choose highly similar signals and a condition for the channels as one group as in [18]. The filter coefficients $h(n)$ are:

$$\mathbf{h}_i = (\mathbf{y}_{N-1})^{-1} y_i \quad (21)$$

where $1 \leq i \leq P$, where P is the number of the similar channels in the group. y_i is the reference channel that will be calibrated. y_{N-1} are all channels except the one that under calibration y_i . h_i is a $(P-1) \times 1$ vector of the filter coefficients used to produce the i th calibration signal.

Using the SVD decomposition method, we can find the filter coefficients h that minimize the least square error. Thus, the calibration signal of the i th received signal can be calculated as:

$$g_i(n) = \sum_{m=1}^{P-1} h_i(m) * y_{N-1}(n, m) \quad (22)$$

Then, the calibrated signals $b \in R^{N \times P}$ are:

$$b(n, i) = y(n, i) - g(n, i) \quad (23)$$

where $1 \leq n \leq N$, and N is the number of samples.

6. IMAGE CONSTRUCTION ALGORITHMS

The UWB radar techniques do not attempt to reconstruct the dielectric-properties profile as in tomography [2], but instead, it is designed to construct the backscattered signal energy as a function of location for identifying the presence and location of significant scatterers in the breast. As mentioned above, several algorithms have been used for image reconstruction, and since our work uses the multistatic manner, we use the approach that supports the multistatic manner and has been shown to have excellent results in the literature such as IDAS [19, 26] in addition to the DAS as a reference:

6.1. Delay And Sum (DAS) Beamforming Algorithm

The following algorithm describes the coherent-sum process adapted from the Synthetic Aperture Radar (SAR) techniques. After sampling the backscattering signal, there will be N samples for each channel. Assume that there are M channels. To form the image, the signals are synthetically focused at each voxel in the breast as an intensity value (I) of the voxel at this location (m) using the formula [27]:

$$I(\vec{r}_m) = \int_0^T \left[\sum_{m=1}^M B_m(\tau_m(\vec{r}_m)) \right]^2 dt \quad (24)$$

where T is the length of the window; B_m is the sampled version of the m th received backscattering signals; \vec{r}_m is the location of the m th focal point; and τ_m is the m th discrete-time delay needed to achieve a synthetic focus of the m th backscatter waveform calculated as:

$$\tau_m(\vec{r}_m) = \frac{D_m}{v\Delta t} \quad (25)$$

where D_m is the distance from the transmitting antenna to the m th focal point and back to the receiving antenna; v is the average velocity of propagation in the breast at the center frequency of the pulse; and Δt is the time-sampling interval.

The focal point is scanned to a new location in the 3-D region of interest, and this process is repeated for each voxel in the 3-D region of interest. In any location, if there is a scatterer, a constructive sum will be there, and if there is no scatterer, a deconstructive sum will result.

6.2. Improved Delay-And-Sum (IDAS) Beamforming Algorithm

Klemm et al. [26] have proposed an improvement for the DAS algorithm. The improved DAS algorithm uses an additional weighting factor QF (Quality Factor), compared to the standard DAS. This factor represents a quality factor of the coherence of the backscattering signal. For each focal point, the quality factor is calculated in three steps. Firstly, a curve of energy collection is plotted during the running of the DAS algorithm calculation. Next, the standard deviation of the energy curve σ_e is calculated by fitting the energy curve to a second-order curve, then the tolerance of the original curve is found about the fitted curve, and the energy collection curve is rescaled by normalizing it to the standard deviation of energy σ_e . Normalization is actually performed using multiplication by $1/(1 + \sigma_e)$ since in an ideal case, $\sigma_e = 0$. This may be thought as a heuristic scaling of the data to a given greater weight to those signals that, following equalization, more closely resemble the desired case of equal energy. In the last step, the

coefficients of a second order polynomial ($y = ax^2 + bx + c$) are estimated by the least-square fitting of the normalized curve of the coherent energy collection. The choice of the second-order polynomial comes from the fact that a curve of the energy collection during a perfect coherent signal summation would follow a quadratic curve because of the relation $10 \log M$. Then, assume that $QF = a$, an order in which the signals are taken should not change the shape of the curve, assuming the perfect equalization. In practice, owing to a non-ideal equalization, the shape of the curve of the energy collection will weakly depend on the order in which signals are summed. However, it has a negligible effect on a value since the final value of the summed energy is constant. The value is calculated using the least-square fitting. Finally, the characteristic equation of the improved DAS algorithm is expressed as in [26] and [28]:

$$I(\vec{r}_m) = QF_m \cdot \int_0^T \left[\sum_{m=1}^M w_m B_m(\tau_m(\vec{r}_m)) \right]^2 dt \quad (26)$$

where QF_m is the quality factor of the m th focal point.

7. TRANSMITTING-RECEIVING ANTENNA SEPARATION DISTANCE

To reduce the late time clutter effect, we identify the channels that have higher reflection power from the target with respect to other backscatters. To do so, we impose distance limitations between the receiving antenna and transmitting antenna. The Transmitting-Receiving Antenna Separation Distance (TRASD) can reduce late time clutters effect and by its rule improve the Signal to Clutter Ratio SCR. The theory that belongs to this proposal is that a good reflection angle from the target cannot go beyond the angle of 180° .

8. SIMULATION AND RESULTS

To verify our method, we use a simulation tool as a reference. Accurate dielectric property measurement of the breast tissue was conducted by Lazebnik et al. [13,14] which can be used to generate a good model as described in [29]. The simulation includes the antennas and the propagation in the breast tissues.

8.1. Antenna

In our simulation, the antenna used is a modified version of our previously published antenna [30]. As shown in Fig. 1(a), the modification includes bending the face of the antenna to be matched with the breast surface. Fig. 1(b) shows the modified antenna return losses. From Fig. 1(b), the antenna is ultra-wideband from 1.9 to 11 GHz, which is more than the working band (3.1–10.6 GHz). This antenna works in contact with the skin and does not has a specific polarization. This antenna has an almost omnidirectional pattern. However, other antennas' types like the directive and polarized antenna described in our previous papers [31, 32] can be used as well.

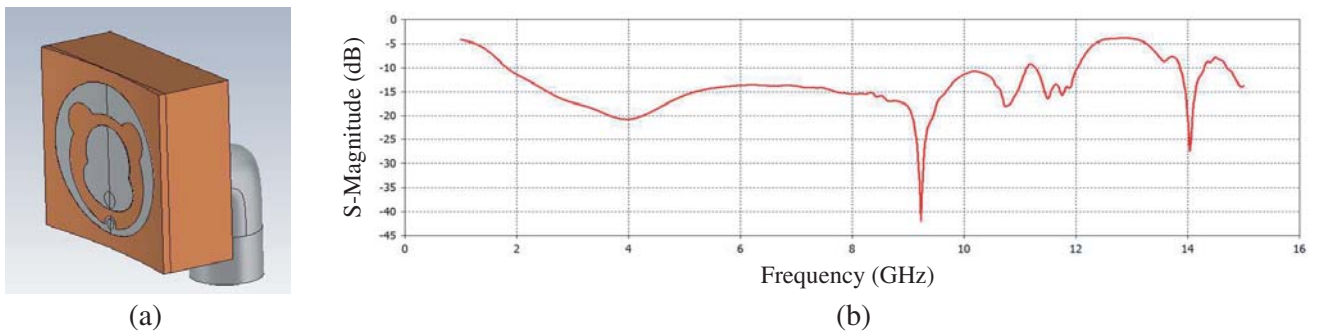


Figure 1. (a) The modified antenna. (b) The signal return loss of the antenna.

8.2. Breast Phantom

Our testing approach supposes that the patient is laying on her chest over a table with two holes at the breast positions. Since we can form the breast in a suitable templet, a cylindrical model is used to get accurate antennas' positions. Also, since we are working on a calibration algorithm, it is required to work on a regular shape like the calibration procedures in the MRI and CAT scanners. However, some complications in the breast phantom have been made with multilayers. The model is shown in Fig. 2. This model consists of 102,763,676 mesh cells. This large number of meshes along with second order fitting of the tissues dielectric properties have led to high memory demand and huge simulation time that was approximately 30 days using a computer with an i7 6th generation CPU core and 16 GB RAM.

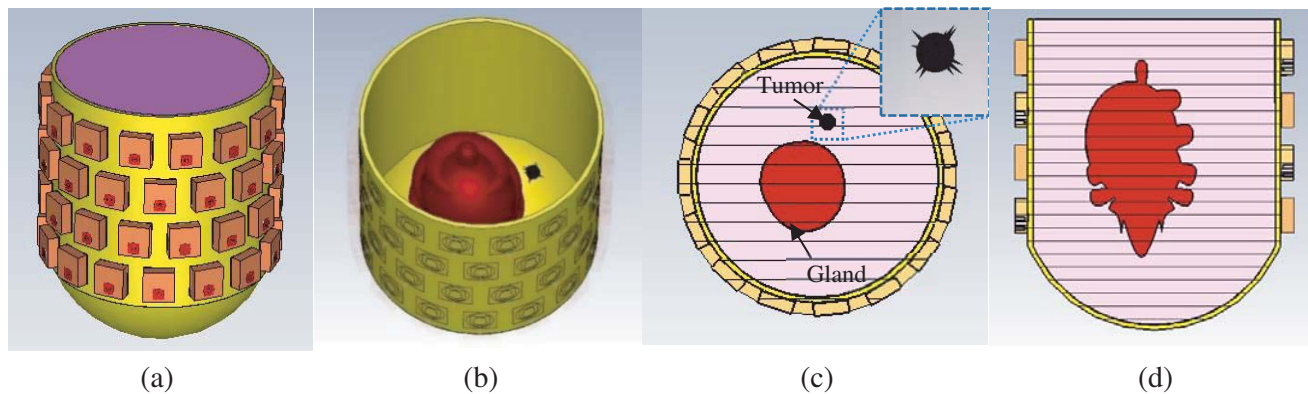


Figure 2. Breast phantom. (a) The entire phantom with the antennas array of 60 elements on it. (b) The gland, tumor and skin. (c) Transversal cross sectional of the breast phantom at the tumor location with zoomed in a close-up of tumor image. (d) Longitudinal cross sectional showing the glandular body.

The multilayers dielectric properties are described by a Cole-Cole model [13, 14]. However, since we need different representations in the simulation tool, the model was changed with second order fitting as discussed in Reference [29]. The phantom is composed of a median-glandular tissue of a random shape having a maximum length of 56 mm and maximum width of 40 mm. The other filling tissues consist of low-fat tissues covered with a 2 mm-thick skin tissue layer on the outside of the phantom. A sphere with 3 mm radius having malignant dielectric properties is placed near the median-glandular body for mimicking the tumor. Also, to make the tumor more realistic, we added cones like needles around it. An in-contact antenna array of 60 elements, described in [30] is used. The antennas are uniformly distributed around the breast in four rings, and each ring is shifted by 15° with respect to the previous ring since this angle forms a diagonal antenna configuration. This diagonal distribution reduces the mutual coupling between the antennas as mentioned in our previous work [30].

An excitation signal of a Gaussian shape and bandwidth of (3.1–10.6) GHz is generated by the simulation tool. A sampling frequency f_s samples the scattered/reflected signals at 1292.2 GHz, and later, these signals will be down sampled to 43 GHz when the algorithms are used.

8.3. Signals Calibration

As discussed in Section 4.1, all signals need calibration to remove the early and late time clutters before applying any beamforming algorithm.

To demonstrate the PI-ESPRIT process details, a signal transmitted from antenna No. 1 and received at antenna No. 2 is used as an example.

Figure 3(b) shows the eigenvalues Σ of Equation (7) for the signal. These eigenvalues represent the signal subspace. The highest values of the eigenvalues represent the most significant subspace where most high power (amplitude) signal sources project on them depending on their power (amplitude) values; therefore, the highest amplitude signals in the received signal represent the major eigenvalues

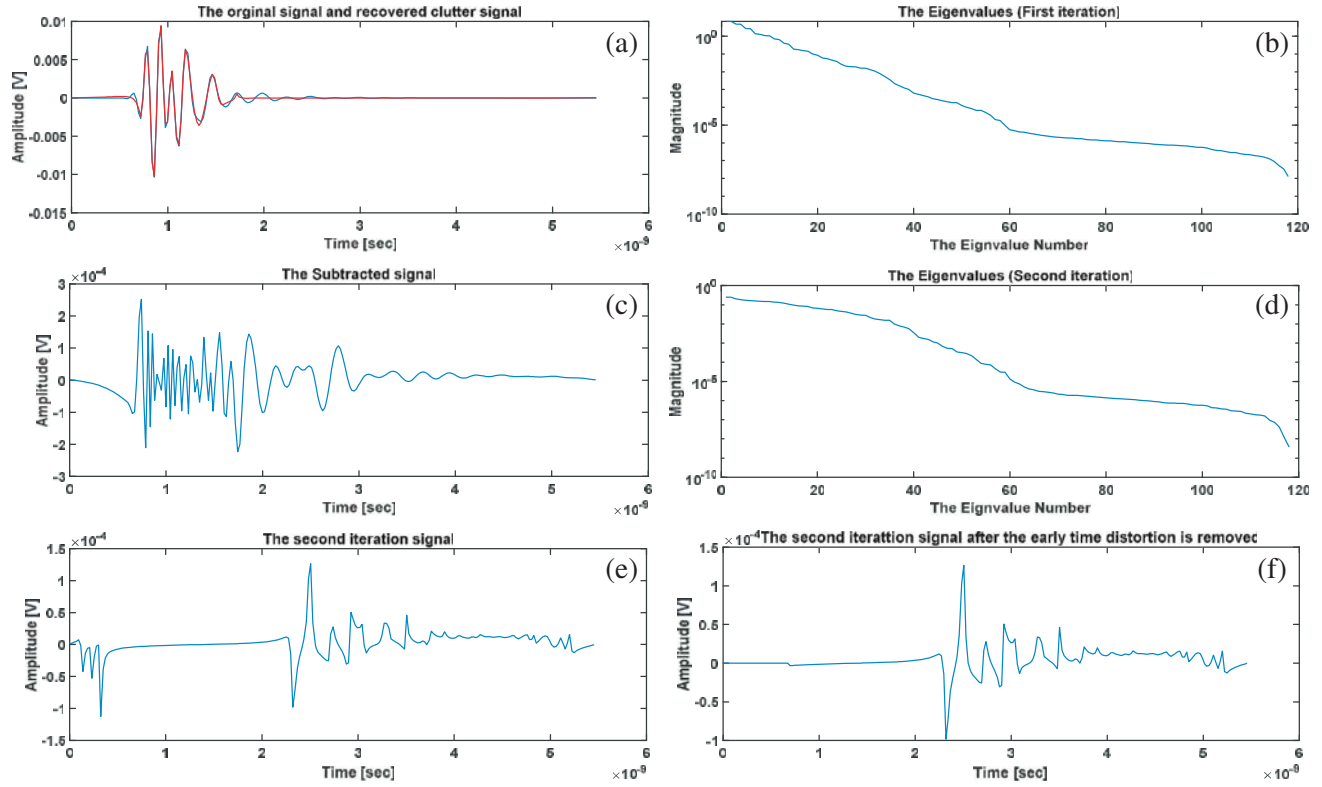


Figure 3. (a) The recovered signal in red color along with original signals in the blue color. (b) The eigenvalues Σ of equation (8) of the first iteration. (c) The resulted signal after subtracting the two signals in (b). (d) The eigenvalues Σ of Equation (8) of the second iteration. (e) The recovered signal in the second iteration. (f) The signal after removing the early distortion caused by the second iteration.

Σ . By recovering the signal using the first 15 eigenvalues from a total of 118 eigenvalues and using the TLS, we can say that we have recovered most of the mutual coupling, outside breast reflections and skin reflections from the signal. However, we can take more than the 15 poles to get perfect identification of the clutter, but this may affect the tumor signal.

Figure 3(a) shows the recovered signal in red color along with original signals in blue color. We can notice the ability of this algorithm in identifying high amplitude clutters signals. After subtracting the recovered signal from the original signal, noise is still generated as shown in Fig. 3(c) because we do not take all the eigenvalues in recovering the signal. Therefore, another iteration of the PI-ESPRIT algorithm is applied, but here, we choose the last 25 eigenvalues and applying LS instead of TLS for recovering the signal of interest that represents back-scattering signals of the tumor and Fibroglandular/Fibroconnection signal. However, the recovered signal from the second iteration also generates some noise at a very early time that can be removed by zeroing their values which will not affect the image since this period essentially represents the early time inside the coaxial cable. Fig. 3(d) shows the eigenvalues' curve which almost keeps its original shape except at the first 15 values that change because of the Poles Isolation and subtraction in the first iteration. Fig. 3(d) shows the recovered signal from the second iteration, and Fig. 3(e) shows the signal after removing the very early time signals. From Fig. 3(e), we see that the early time clutters are completely removed.

For the Wiener filter, we first choose similar channels to be used by the Wiener filter, so to find a calibration signal. This signal should have all the similar signals contained in the group. As shown in Fig. 4(a), the calibration signal is very similar to the original signal; however, when we apply the Wiener filter, it completely fails to identify the high-power backscatters. This failure can be seen clearly after subtracting the calibration signal from the original signal. As shown in Fig. 4(b), the subtracted signal still has the early time clutter dominant with some visibility of the gland and tumor signals directly after this clutter.

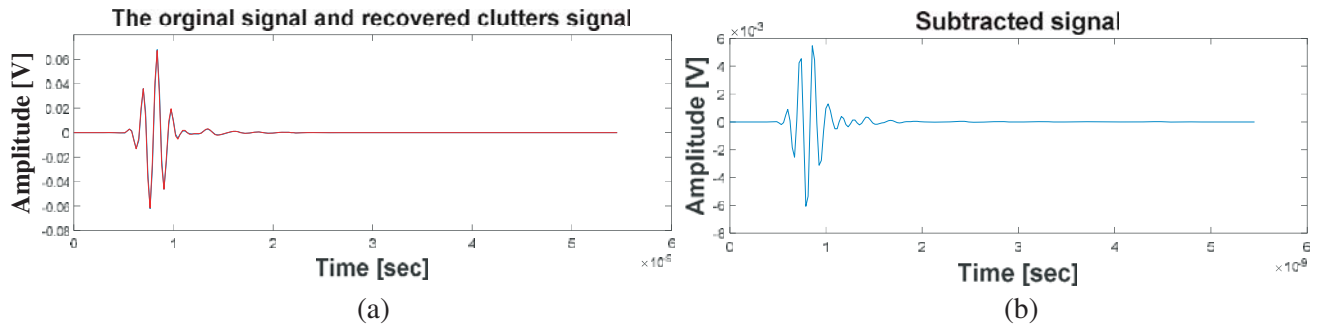


Figure 4. (a) The recovered signal using the Wiener filter in red color along with original signals in the blue color. (b) The subtracted signal.

8.4. Image Construction

For image construction and tumor detection, a program utilizes the ESPRIT calibration algorithm along with DAS and IDAS beamformers discussed in Sections 6.1 and 6.2, respectively. In this program, for beamforming algorithm calculations, the phantom is considered to be composed of a homogeneous material having an averaging value of ϵ_r . An average value of $\epsilon_r = 6.8$ for the relative dielectric is used, where we calculate an average value on the path of electromagnetic propagation through the skin and fat

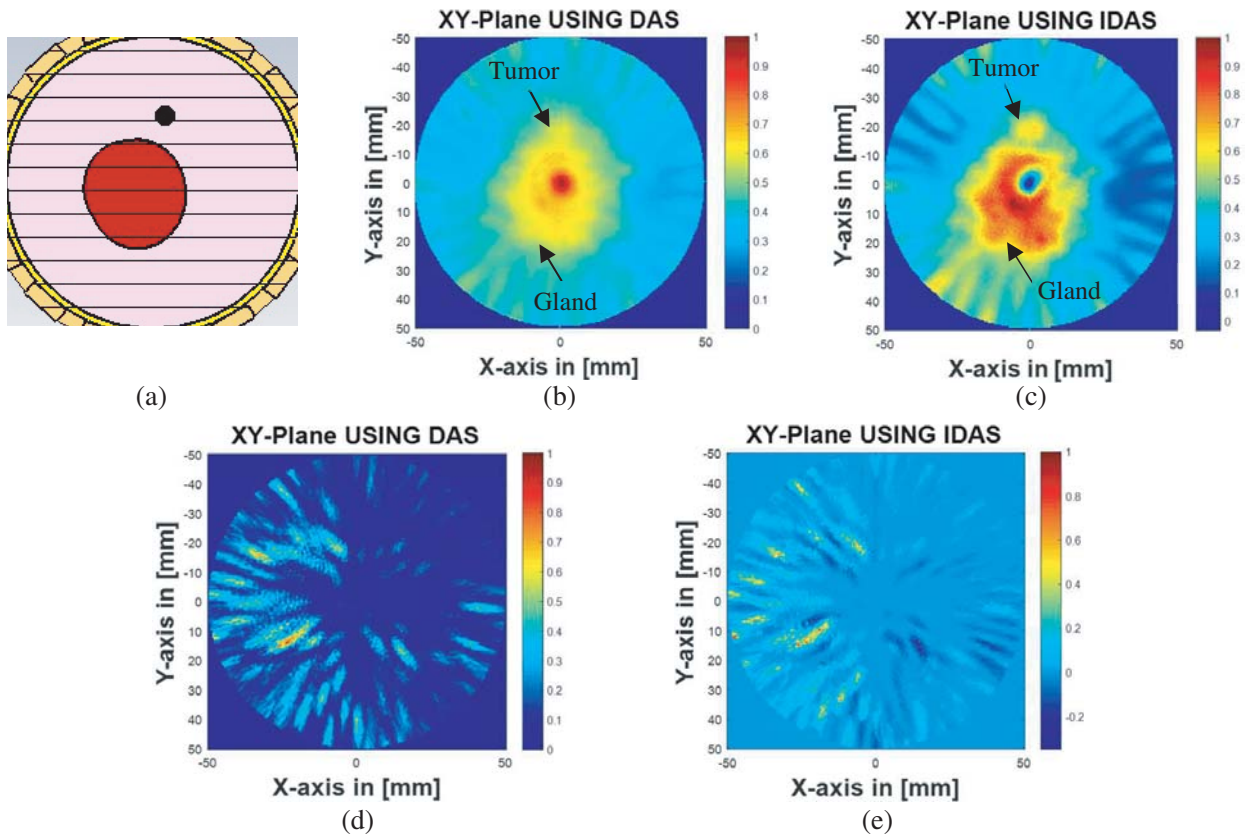
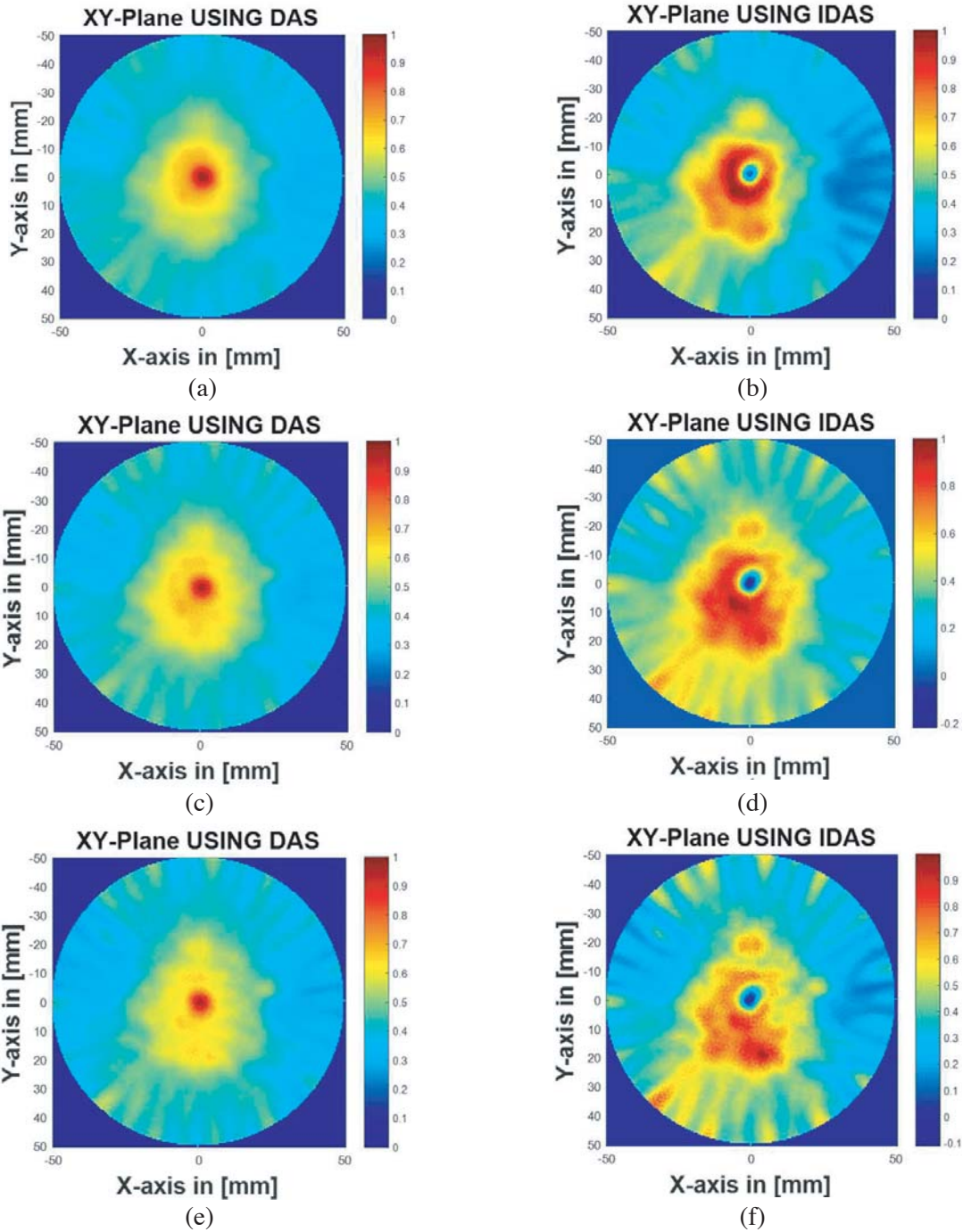


Figure 5. (a) Across section in the XY-plane at the tumor location of the original phantom. (b) The image is generated by the PI-ESPRIT algorithm with DAS. (c) The image is generated by the PI-ESPRIT algorithm with IDAS. (d) The image is generated by the Wiener filter with DAS. (e) The image is generated by the Wiener filter with IDAS.

tissue (where the relative dielectric ϵ_r of low-fat tissue is 3.68 at the center frequency 6.85 GHz and 36 for skin tissue, and by integrating the two values on the path of 2 mm skin and 19 mm fat and dividing the result on the sum of two distances of 21 mm, we get roughly the average 6.8 for ϵ_r). Fig. 5(a) shows a cross-section in the XY -plane at the tumor location of the original phantom. Fig. 5(b) shows the image using the ESPRIT algorithm with DAS, and Fig. 5(c) shows the image using the ESPRIT algorithm with IDAS. From these figures, we find that the ESPRIT algorithm with IDAS beamforming outperforms the ESPRIT algorithm with DAS beamforming in the sense of signal to clutter ratio. Although there are some clutters caused by averaging the speed of light over the entire geometry of the breast. The algorithm shows good image reconstruction ability with the existence of a large amount of glandular



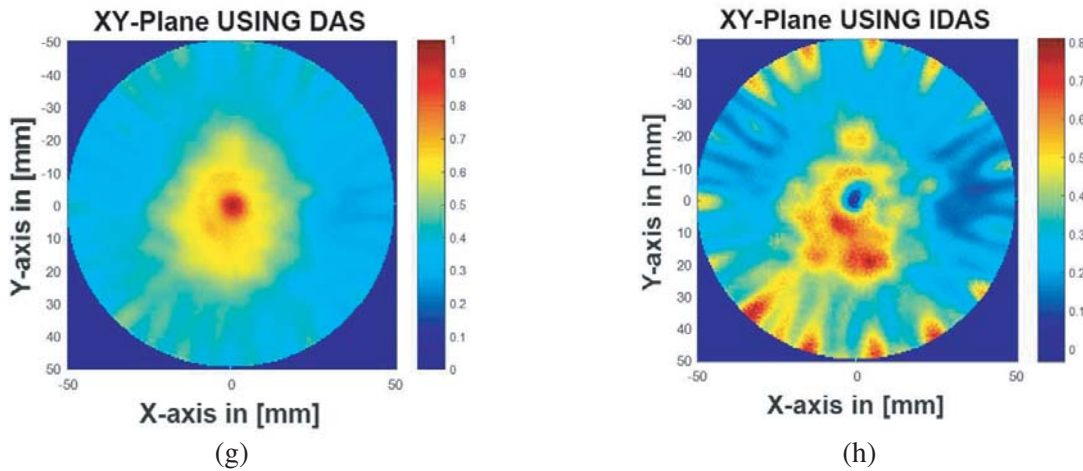


Figure 6. The signals in these images were calibrated using PI-ESPRIT algorithm and the images were constructed using either DAS or IDAS with different TRASD: (a) DAS and 0.052 m TRASD; (b) IDAS and 0.052 m TRASD; (c) DAS and 0.06 m TRASD; (d) IDAS and 0.06 m TRASD; (e) DAS and 0.08 m TRASD; (f) IDAS and 0.08 m TRASD; (g) DAS and no use of TRASD condition; (h) IDAS and no use of TRASD condition.

tissue. To compare our algorithm with another well-known one, we use the Wiener filter as described in Section 6. As shown in Figs. 5(d) and 5(e), the Wiener filter fails to calibrate the signals, and there is no image in the DAS and IDAS beamformers, respectively.

Figures 5(a) to 5(e) are generated using 0.07 m TRASD, as mentioned in Section 7. To see the effect of the TRASD on image quality and clutters reduction, we generate images in Figures 6(a), 6(b), 6(c), 6(d), 6(e), and 6(f) using three values [0.052 m, 0.06 m, 0.08 m] of TRASD. Generally, as can be concluded from these figures, it is clear that as the value of the separation increases, the clutter power increases, but the tumor gland images become clearer. We can modify TRASD value to find the best image. Figs. 6(g) & 6(h) show the images using all 1770 channels. As can be observed from the figure, using all of the channels, one can see the increase of clutter power; conversely, the tumor image becomes clearer, but the gland image degrades. Regarding changing TRASD using the Wiener filter, since the Wiener filter fails to calibrate the signals, we do not show any further image about changing the TRASD value effect.

9. CONCLUSION

In this paper, we introduce the application of the ESPRIT algorithm for the calibration of multistatic signals in the microwave breast cancer imaging and detection based on Ultra-Wide Band (UWB) Radar Imaging. This approach uses the ESPRIT algorithm to remove the high-power backscatters coming from the mutual coupling among the antennas, skin reflections, outside breast backscatters, and inside antenna oscillation. Reconstruction image algorithms DAS and IDAS are used. We compare our approach with the Wiener filter calibration since it is considered one of the best approaches for signal calibration in microwave breast cancer detection. The PI-ESPRIT algorithm shows the ability to identify and remove high amplitude clutter signals and recover the tumor signal. However, the Wiener filter shows a complete failure in this study. It is also clear that the IDAS algorithm gives better results than the DAS algorithm in image construction and clutters levels. Finally, to reduce late time clutters, we propose the use of Transmitting-Receiving Antenna Separation Distance (TRASD) to limit the angle of reflections from the target at a specific voxel and to collect the channels that have higher information related to the voxel under calculation than other voxels in the breast. By numerical tests, we find that this assumption is correct, and the best transmitting-receiving antennas separation distance in our phantom is 0.07 m.

REFERENCES

1. Donelli, M., I. J. Craddock, D. Gibbins, and M. Sarafianou, "A three-dimensional time domain microwave imaging method for breast cancer detection based on an evolutionary algorithm," *Progress In Electromagnetics Research M*, Vol. 18, 179–195, 2011.
2. Rahama, Y. A., O. A. Aryani, U. A. Din, M. A. Awar, A. Zakaria, and N. Qaddoumi, "Novel microwave tomography system using a phased-array antenna," *IEEE Transactions on Microwave Theory and Techniques*, Vol. 66, No. 11, 5119–5128, 2018.
3. Caorsi, S., M. Donelli, A. Lommi, and A. Massa, "Location and imaging of two-dimensional scatterers by using a particle swarm algorithm," *Journal of Electromagnetic Waves and Applications*, Vol. 18, No. 4, 481–494, 2019.
4. Mahmud, M. Z., M. T. Islam, N. Misran, S. Kibria, and M. Samsuzzaman, "Microwave imaging for breast tumor detection using uniplanar AMC based CPW-fed microstrip antenna," *IEEE Access*, Vol. 6, 44763–44775, 2018.
5. Fear, E. C., X. Li, S. C. Hagness, and M. A. Stuchly, "Confocal microwave imaging for breast cancer detection: Localization of tumors in three dimensions," *IEEE Trans. Biomed. Eng.*, Vol. 49, No. 8, 812–822, 2002.
6. Hagness, S. C., A. Taove, and J. E. Bridges, "Two-dimensional FDTD analysis of a pulsed microwave confocal system for breast cancer detection: Fixed focus and antenna array sensors," *IEEE Trans. Biomed. Eng.*, Vol. 45, No. 12, 1470–1479, 1998.
7. Bond, E. J., X. Li, S. C. Hagness, and B. van Veen, "Microwave imaging via space-time beamforming for early detection of breast cancer," *IEEE Trans. Ant. Propag.*, Vol. 51, No. 8, 1690–1705, 2003.
8. Williams, T. C., E. C. Fear, and D. T. Westwick, "Tissue sensing adaptive radar for breast cancer detection — Investigations of an improved skin-sensing method," *IEEE Transactions on Microwave Theory and Techniques*, Vol. 54, No. 4, 1308–1314, Apr. 2006.
9. O'Halloran, M., M. Glavin, and E. Jones, "Channel-ranked beamformer for the early detection of breast cancer," *Progress In Electromagnetics Research*, Vol. 103, 153–168, 2010.
10. Nilavalan, R., A. Gbedemah, I. J. Craddock, X. Li, and S. C. Hagness, "Numerical investigation of breast tumor detection using multi-static radar," *IEE Electronics Letters*, Vol. 39, No. 25, Dec. 11, 2003.
11. Lim, H., N. Nhung, E. Li, and N. Thang, "Confocal microwave imaging for breast cancer detection: Delay-multiply-and-sum image reconstruction algor," *IEEE Trans. Biomed. Eng.*, Vol. 55, No. 6, 1697–1704, Jun. 2008.
12. Yin, T., F. H. Ali, and C. C. Reyes-Aldasoro, "A robust and artifact resistant algorithm of ultrawideband imaging system for breast cancer detection," *IEEE Trans. Biomed. Eng.*, Vol. 62, No. 6, 1514–1525, 2015.
13. Lazebnik, M., L. McCartney, D. Popovic, C. B. Watkins, M. J. Lindstrom, J. Harter, S. Sewall, A. Magliocco, J. H. Booske, M. Okoniewski, and S. C. Hagness, "A large-scale study of the ultra-wideband microwave dielectric properties of normal breast tissue obtained from reduction surgeries," *Phys. Med. Biol.*, Vol. 52, 2637–2656, 2007.
14. Lazebnik, M., D. Popovic, L. McCartney, C. B. Watkins, M. J. Lindstrom, J. Harter, S. Sewall, T. Ogilvie, A. Magliocco, T. M. Breslin, W. Temple, D. Mew, J. H. Booske, M. Okoniewski, and S. C. Hagness, "A large-scale study of the ultra-wideband microwave dielectric properties of normal, benign and malignant breast tissues obtained from cancer surgeries," *Phys. Med. Biol.*, Vol. 52, No. 20, 6093–6115, Oct. 2007.
15. Maskooki, A., E. Gunawan, C. B. Soh, and K. S. Low, "Frequency domain skin artifact removal method for ultra-wideband breast cancer detection," *Progress In Electromagnetics Research*, Vol. 98, 299–314, 2009.
16. Zhi, W. and F. Chin, "Entropy-based time window for artifact removal in UWB imaging of breast cancer detection," *IEEE Signal Processing Letters*, Vol. 13, No. 10, 585–588, 2006.

17. Elahi, M. A., A. Shahzad, M. Glavin, E. Jones, and M. O'Halloran, "Hybrid artifact removal for confocal microwave breast imaging," *IEEE Antennas and Wireless Propagation Letters*, Vol. 13, 1–4, 2014.
18. Song, H., Y. Li, and A. Men, "Microwave breast cancer detection using time-frequency representations," *MBEC*, Vol. 56, No. 4, 571–582, 2018.
19. Shaheen, A. M. A. and K. M. Quboa, "Pole splitting algorithm For UWB breast cancer imaging," *2012 16th IEEE Mediterranean Electrotechnical Conference (MELECON)*, Yasmine Hammamet, 2012.
20. Cuomo, K., J. Piou, and J. Mayhan, "Ultrawide-band coherent processing," *IEEE Microwave Magazine*, Vol. 47, No. 6, 1094–1107, 1999.
21. Papy, J.-M., L. De Lathauwer, and S. van Huffel, "Common pole estimation in multi-channel exponential data modeling," *Signal Processing*, Vol. 86, 846–858, 2005.
22. Papy, J.-M., L. De Lathauwer, and S. van Huffel, "Exponential data fitting using multilinear algebra: The decimative case," *J. Chemometrics*, Vol. 23, 341–351, 2009.
23. Lazaro, A., D. Girbau, and R. Villarino, "Simulated and experimental investigation of microwave imaging using UWB," *Progress In Electromagnetics Research*, Vol. 94, 263–280, 2009.
24. Elahi, M. A., M. Glavin, E. Jones, and M. O'Halloran, "Artifact removal algorithms for microwave imaging of the breast," *Progress In Electromagnetics Research*, Vol. 141, 185–200, 2013.
25. Yin, T., F. H. Ali, and C. C. R. Aldasoro, "A robust and artifact resistant algorithm of ultrawideband imaging system for breast cancer detection," *IEEE Trans. Biomed. Eng.*, Vol. 62, No. 6, 1–12, 2015.
26. Klemm, M., I. J. Craddock, J. A. Leendertz, A. Preece, and R. Benjamin, "Improved delay-and-sum beamforming algorithm for breast cancer detection," *International Journal of Antennas and Propagation*, Vol. 2008, 2008.
27. Zhuge, X., M. Hajian, A. G. Yarovoy, and L. P. Ligthart, "Ultra-wideband imaging for detection of early-stage breast cancer," *Proceedings of the 4th European Radar Conference*, Munich, Germany, Oct. 2007.
28. O'Halloran, M., M. Glavin, and E. Jones, "Effects of fibroglandular tissue distribution on data-independent beamforming algorithms," *Progress In Electromagnetics Research*, Vol. 97, 141–158, 2009.
29. Shaheen, A. M. A. and K. M. Quboa, "Development of accurate UWB dielectric properties dispersion at CST simulation tool for modeling microwave interactions with numerical breast phantoms," *The Eighth International Multi-Conference on Systems, Signals & Devices (SSD 11)*, Sousse, Tunisia, 2011.
30. Shaheen, A. M. A. and K. M. Quboa, "Modeling and optimizing ultra wideband antennas for microwave breast cancer detection," *International Multi-Conference on Systems, Signals & Devices*, Chemnitz, Germany, 2012.
31. Al-Zuhairi, D. T., J. M. Gahl, and N. E. Islam, "Compact dual-polarized quad-ridged UWB horn antenna design for breast imaging," *Progress In Electromagnetics Research C*, Vol. 72, 133–140, 2017.
32. Al-Zuhairi, D., J. M. Gahl, A. M. Abed, and N. E. Islam, "Characterizing horn antenna signals for breast cancer detection," *Canadian Journal of Electrical and Computer Engineering*, Vol. 41, No. 1, 8–16, 2018.